

Compressing and forecasting atomic material simulations with descriptors

Thomas. D. Swinburne*

Aix-Marseille Université, CNRS, CINaM UMR 7325, Campus de Luminy, 13288 Marseille, France

(Dated: September 6, 2023)

Atomic simulations of material microstructure require significant resources to generate, store and analyze. Here, atomic descriptor functions are proposed as a general latent space to compress atomic microstructure, ideal for use in large-scale simulations. Descriptors can regress a broad range of properties, including character-dependent dislocation densities, stress states or radial distribution functions. A vector autoregressive model can generate trajectories over yield points, resample from new initial conditions and forecast trajectory futures. A forecast confidence, essential for practical application, is derived by propagating forecasts through the Mahalanobis outlier distance, providing a powerful tool to assess coarse-grained models. Application to nanoparticles and yielding of dislocation networks confirms low uncertainty forecasts are accurate and resampling allows for the propagation of smooth microstructure distributions. Yielding is associated with a collapse in the intrinsic dimension of the descriptor manifold, which is discussed in relation to the yield surface.

Materials evolve via complex, non-intuitive atomic mechanisms spanning a wide range of time and length scales[1, 2]. Atomic simulations (MD) with empirical force fields offer exceptional insight, but although spatial decomposition schemes give excellent (weak) parallel scaling with system size[3], serial time integration limits trajectory duration, irrespective of available processors[4]. The ubiquity yet high cost of MD means development of predictive techniques to coarse-grain (CG) in space or time is an active research area [2, 5–9]. Material microstructure requires large system sizes, necessitating efficient and scalable CG techniques. Whilst many structural analysis tools exist[10–15], none provide generic *compression* of atomic data with a clear metric for similarity or diversity, nor is it clear *a priori* how to select CG properties, leading to massive storage requirements at scale[16, 17]. A further challenge is that simulations of materials are typically non-equilibrium and exhibit, in part due to timescale limitations, partially disordered structures with a dense kinetic spectrum and an unknown steady state, often with external driving[18–20]. To harness modern parallel computers there is thus a recognized need to *resample* sparse simulation data and to *forecast* simulation futures, both for physical insight and to maximize the information yield of additional computational effort[4, 21–25].

However, the complexities of material deformation limit the applicability of current CG and acceleration schemes, which require identification of a clear timescale separation[26] to allow parallel time accumulation[2, 4, 9, 21, 26–29] or the design of low rank (typically 1-4) collective variables (CV) which can be used to bias dynamics [5, 8, 30–34]. Despite many recent advances[8, 35, 36] general CVs for microstructure remain elusive[34, 36], instead requiring specialized simulation setups with only a few active mechanisms such as nucleation[8] or the migration of isolated defects[34, 35]. Exploring *unseen* regions of configuration space is known to be uncontrolled as low rank CVs may not remain descriptive[37].

These issues extend to the powerful post-mortem analysis tools[6, 38–42], which learn collective variables that obey a discrete state Markov model in order to identify kinetically important configurations with implied transition timescales. Whilst all-atom[43–46] or coarse-beaded[47] generative models may provide a route for accelerated time-stepping, they are currently only competitive to direct time integration for fairly small equilibrium systems with a static or slowly varying bonding topology and so cannot be applied to large-scale simulations of material deformation where a highly transient, heterogeneous atomic connectivity is fundamental.

In this contribution, atomic descriptor functions [48–52] are proposed as an efficient, general and uncertainty-aware coarse-graining approach, mapping atomic positions $\mathbf{X} \in \mathbb{R}^{N \times 3}$ to a global vector $\mathbf{D} \in \mathbb{R}^{\sim 100}$, Eq. 1. The main results are that 1) Descriptors can classify and regress a remarkable range of microstructural properties (see figures) and permit a data-driven model extrapolation measure[53], transferring advances in active learning [54–56] to atomic CG. This generality means CG targets need not be specified *a priori*, giving huge compression in storage and efficiencies in analysis at scale. 2) Descriptor trajectories can be efficiently resampled and forecasted via a vector autoregressive (VAR) model [57], with, crucially, a robust forecast *uncertainty* derived from the descriptor outlier measure (5). This allows rapid assessment of when forecasts can be trusted or when additional training is needed, essential for practical usage but typically missing in existing schemes. The approach is applied to analyze and forecast systems essentially untreatable with existing methods, the annealing of large nanoparticles and dislocation yielding under cyclic shear and uniaxial tension[17]. Yielding is identified with a collapse in the intrinsic dimension[58] of the descriptor manifold.

Descriptor coarse-graining of microstructure
Descriptors[56, 60–62] map atomic coordinates $\mathbf{X} \in \mathbb{R}^{N \times 3}$ to $\mathbf{D}(\mathbf{X}) \in \mathbb{R}^{N \times D}$, where each element

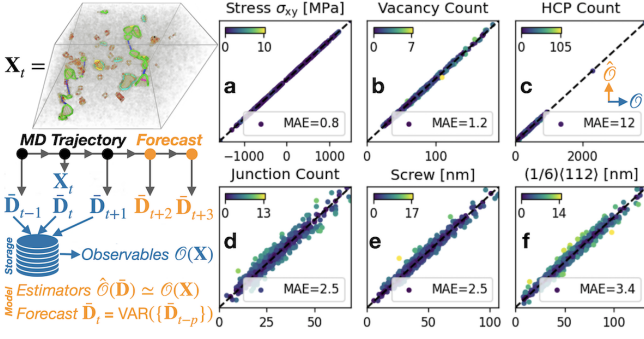


FIG. 1. Coarse graining of dislocation networks in Al under cyclic shear, detailed in the SM[59]. Left: Global descriptor vectors $\bar{\mathbf{D}}$ (1) are stored every 1-10ps and positions \mathbf{X} every 100-500ps. $\{\mathbf{X}, \bar{\mathbf{D}}\}$ data is used to train estimators $\hat{\mathcal{O}}(\bar{\mathbf{D}})$ of observables $\mathcal{O}(\mathbf{X})$ and a VAR forecaster (8). a-f) : \mathcal{O} vs $\hat{\mathcal{O}}$ from over 20 targets, including d) dislocation junctions and total length of e) screw or f) $\langle 112 \rangle / 6$ dislocations. Non-scalar a) σ_{xy} , estimated with $\bar{\mathbf{D}} \oplus \bar{\mathbf{V}}$ [59]. See also $g(r)$ in Fig. 2.

$[\mathbf{D}(\mathbf{X})]_{ij}$ takes the local atomic environment of an atom i as input and returns a permutation-invariant scalar, vector or tensor depending on the regression target (e.g. energies, forces)[63, 64]. Descriptors which approximate a many-body atomic basis[48–52] have found use in *linear* estimators $\hat{\mathcal{O}} \simeq \Theta_{\mathcal{O}} \cdot \bar{\mathbf{D}} + \Theta_{\mathcal{O}}^0$ of some target observable $\mathcal{O}(\mathbf{X})$, where $\Theta_{\mathcal{O}} \in \mathbb{R}^D$ and $\Theta_{\mathcal{O}}^0 \in \mathbb{R}$ are parameters. For $\mathcal{O} = E$, the atomic potential energy, these can reach state of the art accuracy[61, 64, 65], often with lower computational cost and simpler fitting[48–52]. The first main result of this contribution is that linear estimators can capture essentially any microstructural property which could be of relevance to a coarse grained model. The widely used[3] bSO(4) descriptors[3, 48, 50, 65] are used, detailed in the supplementary material (SM)[59], summing over all atoms to give the global descriptors

$$\bar{\mathbf{D}} = \sum_i \mathbf{D}_i \in \mathbb{R}^D, \bar{\mathbf{V}} = \sum_i \mathbf{X}_i \otimes \nabla_{\mathbf{X}} \mathbf{D}_i \in \mathbb{R}^{D \times 3 \times 3}, \quad (1)$$

where \otimes is the outer (dyadic) product[66]. Figure (1) shows linear estimators

$$\hat{\mathcal{O}}(\bar{\mathbf{D}}) = \Theta_{\mathcal{O}} \cdot \bar{\mathbf{D}} + \Theta_{\mathcal{O}}^0, \quad (2)$$

applied to dislocation networks in aluminum[59], accurately capturing a broad range of properties including dislocation junction densities, character-dependent line densities and crystal structure content. Similar results were found for the nanoparticle ensemble and a range of dislocated solids in fcc and bcc materials. Dislocation properties were extracted with OVITO-DXA[15] which has some intrinsic noise due to the discretization parameters. It is also possible to capture the radial distribution function (RDF) $g(r)$ by estimating coefficients $\hat{a}_l(\bar{\mathbf{D}})$ of a basis expansion $g(r) \equiv \sum_l a_l u_l(r)$, as shown in Fig. 2. As found in previous work targeting

vibrational entropies[67, 68], all predictions were stable under widely varying test/train ratios and truncation of training data range. Matrix-valued observables such as the stress $\mathcal{O}(\mathbf{X}) = \boldsymbol{\sigma} \in \mathbb{R}^{3 \times 3}$ can be estimated by building equivariant estimators with $\bar{\mathbf{V}}$; the simplest ($l = 0$ [64]) example is simply $\hat{\mathcal{O}}(\bar{\mathbf{D}}) = \Theta_{\mathcal{O}} \cdot \bar{\mathbf{V}} \in \mathbb{R}^{3 \times 3}$. Examples for the non-scalar shear stress σ_{xy} are shown in figure (1) and the SM[59]. However, in the following only $\bar{\mathbf{D}}$ is used for forecasting, targeting the scalar pressure $\text{Tr}(\boldsymbol{\sigma})$, as model parameters are scalars and $\bar{\mathbf{D}}$ has a metric distance[48]. Whilst (2) is trained on the global descriptor signal (1), the same procedure can be applied to spatially-dependent signal from atoms in some voxel discretization. Further investigation of this spatially dependent signal and constraints required for any forecast will be the subject of a future contribution. The accuracy and scope of (2) has particular relevance for massively parallel workflows, as only $\bar{\mathbf{D}}, \bar{\mathbf{V}}$ need to be stored to later extract almost any global observable of interest *a posteriori* after training on a small database of stored positions, offering massive data compression.

Unimodality and generation of descriptor data As the descriptors have a metric distance, similar microstructures will be close in descriptor space. In addition, their distribution in sufficiently high dimension can be expected to be unimodal, routinely invoked in active learning schemes [54, 55] and more recently in the analysis of defect structures[56]. Evidence for nanoparticle and dislocation ensembles is provided in the SM[59]. It is then simple to *generate* plausible descriptor vectors by fitting and sampling a multivariate normal distribution $\mathcal{N}(\boldsymbol{\mu}, \boldsymbol{\Sigma})$ to the descriptor dataset. An example of this is shown below in figure 3, where the observed descriptor initial conditions are densely interpolated, allowing the evolution of observable distributions to be monitored.

Resampling and forecasting of descriptor trajectories At regular intervals $t_n = n\delta\tau$, $\delta\tau \simeq 10\text{ps}$, a ‘snapshot’ is taken by time averaging $\bar{\mathbf{X}}_n = \tau_D^{-1} \int_0^{\bar{\tau}} \mathbf{X}(t_n + t) dt$ over a period $\bar{\tau} \simeq 20 - 50\text{fs}$ to reduce noise from thermal fluctuations[69], then calculating descriptor vectors $\bar{\mathbf{D}}_n = \bar{\mathbf{D}}(\bar{\mathbf{X}}_n)$. A small database of positions $\bar{\mathbf{X}}_n$ is built by recording 1 – 5% of snapshots, though positions could be selected adaptively to maximise training diversity. An ensemble of M simulations thus produces M discrete time trajectories $\{\bar{\mathbf{D}}_n\}$, which are used to train a P -state vector autoregressive VAR(P) model[57, 70]

$$\bar{\mathbf{D}}_{n+1} = \sum_{p=0}^{p=P-1} \mathbf{T}_p \bar{\mathbf{D}}_{n-p} + \mathbf{c} + \mathbf{w}_n, \langle \mathbf{w}_n^\top \mathbf{w}_m \rangle = \mathbf{S} \delta_{nm}. \quad (3)$$

For $P > 1$ a Wold transformation[71] $\mathbf{Z}_n = \mathbf{1} \oplus \bar{\mathbf{D}}_n \cdots \oplus \bar{\mathbf{D}}_{n-p} \in \mathbb{R}^{1+P\bar{D}}$ casts (8) as a Markovian Ornstein-Uhlenbeck equation[72] $\mathbf{Z}_{n+1} = \mathbf{T}\mathbf{Z}_n + \mathbf{W}_n$. The maximum likelihood estimator of \mathbf{T} is simply the

least squares solution, with \mathbf{S} determined from the residual covariance[70]. To minimize generalization error a bagging[73–75] approach was developed, applying Bayesian ridge regression[76] to random overlapping subsets. Results were stable under 10-40 subsets each with 10-40% coverage, giving epistemic uncertainties $\delta\mathbf{T}$, $\delta\mathbf{S}$ from the covariance across subsets. Training is robust and requires only a few CPU minutes, a key advantage over (RNN/LSTM) neural networks[77, 78] or neural differential equations[79] which require significant resources, regularisation/correction schemes[47], and limited in practice to data dimension $\tilde{D} < 10$ [79, 80]. A Chapman-Komologorov test[6] for the transfer matrix \mathbf{T} is provided in the SM[59], but in practice the light computational demand also permits a convergence test of model architecture by increasing P [59].

Deriving a forecast uncertainty Practical application of (8) requires a robust measure of forecast uncertainty[4, 21–25], which should be larger for configurations further from the training data independent of epistemic errors. This is particularly relevant to the non-stationary dynamics of material deformation. As uncertainty to previously unseen macroscopic changes is clearly not quantifiable[21], the following bound is conditional on the simulation *ensemble* remaining unimodal and not undergoing macroscopic changes. Many extrapolation grade estimators have been developed for active learning of energy models[54, 56, 58, 65, 81]; here, the Mahalanobis outlier distance[53] is used for the unimodal descriptor distribution[56, 59]. With training data mean $\boldsymbol{\mu}_{\text{tr}}$ and covariance $\boldsymbol{\Sigma}_{\text{tr}}$ estimated via a shrinkage estimator[82], the squared Mahalanobis distance reads

$$\mathcal{M}(\bar{\mathbf{D}}) = [\bar{\mathbf{D}} - \boldsymbol{\mu}_{\text{tr}}] \boldsymbol{\Sigma}_{\text{tr}}^{-1} [\bar{\mathbf{D}} - \boldsymbol{\mu}_{\text{tr}}] / \tilde{D}. \quad (4)$$

Importantly, (12) is independent of the VAR(P) forecast model (8); points drawn from a low density region of ρ_{tr} will have a large Mahalanobis distance, even if epistemic uncertainties $\delta\mathbf{T}$ are small. At long forecasting times, (8) will reach its high dimensional steady state[59], with $\langle \mathcal{M} \rangle$ constant. However, model parameters cannot be assumed static, with a time dependence bounded from below by $1/\tau_M = 1/(M\tau_{\text{tr}})$ [83], where M is the ensemble size and τ_{tr} training duration. This drift can be estimated by propagating epistemic uncertainty in the steady state to an uncertainty $\sigma_{\mathcal{M}}^2$ in $\mathcal{M}(\bar{\mathbf{D}})$, which should be accumulated[59], leading to an additional linear growth in (12) of

$$\mathcal{M}(t_n) = \langle \mathcal{M}(\bar{\mathbf{D}}_n) \rangle + \mathcal{M}_{\sigma}(t_n), \quad \mathcal{M}_{\sigma}(t_n) \geq \mathcal{M}_0(t_n). \quad (5)$$

where $\mathcal{M}_{\sigma}(t) = \sigma_{\mathcal{M}}^2 t / \delta\tau$ and $\mathcal{M}_0(t) = t / \tau_M$. Equation (5) is the main theoretical result of this contribution, an uncertainty metric for forecasting via (8). An approximate parallel efficiency is implied by $\eta = \tau_{\text{pred}} / (M\tau_{\text{tr}})$, where $\mathcal{M}(\tau_{\text{pred}}) \equiv \mathcal{M}_0(M\tau_{\text{tr}}) = 2$, giving $\eta = 1$ when $\mathcal{M}(t_n) = \mathcal{M}_0(t)$.

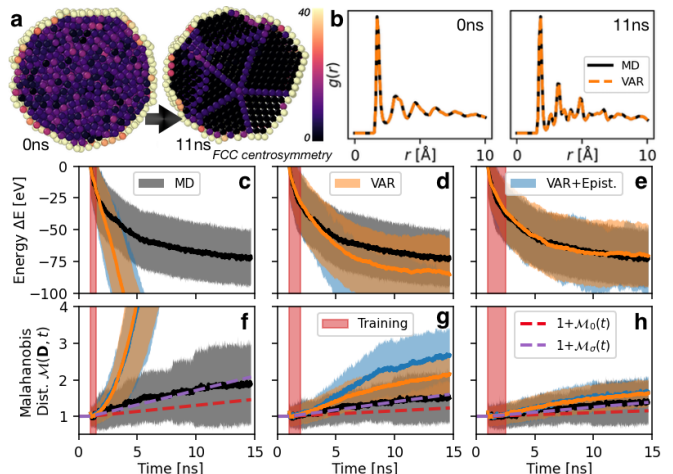


FIG. 2. Annealing of Pt nanoparticles. a) Representative structure at 0,11ns. b) The average RDF $g(r)$ and the corresponding descriptor estimation[59] $g(r; \bar{\mathbf{D}})$. c)-h) Ensemble data with $M = 60$, $\tau_{\text{tr}} = 0.5, 1.0, 1.5\text{ns}$, training starting at $t = 1\text{ns}$ (left-right, red shade). Mean is solid line, with standard deviation as bands. Black: MD data. Orange: VAR forecasts from 1ns. Blue: VAR forecast with epistemic errors. c)-e) Potential energy change from 1ns mean. f)-h) Mahalanobis distances, MD: $\mathcal{M}(\bar{\mathbf{D}}_t)$, eq. (12), forecasts: $\mathcal{M}(t)$, eq. (5). The theoretical lower bounds \mathcal{M}_0 (red dash) and \mathcal{M}_{σ} (purple dash) are also shown.

Annealing of Pt Nanoparticles Metallic nanoparticles are important functional materials for catalysis; 50-150 atom clusters have been extensively studied in simulations[1, 39, 40, 84], but for large sizes and high temperatures the landscape of energy minima is vast and insufficiently metastable for current acceleration methods[40]. The current application to $M = 60$ 4000-atom EAM-Pt[85] nanoparticles at 900K is thus untreatable with existing methods.

The initial structure was formed by quenching from the liquid state and annealing for 100ps to give a highly disordered but predominantly fcc structure ($c_{\text{FCC}} \simeq 0.5$). Descriptor trajectories were extracted every 1.5 ps, with a full structural analysis undertaken every 100ps, though the dataset was sparsified by taking $\delta\tau = 15\text{ps}$ and removing intermediate snapshots. Autoregressive models (8) were constructed with $P = 1 - 3$ and $\tau_{\text{tr}} = 0.5, 1.0$ or 1.5ns , with $P = 1$ shown. Generated trajectories were launched from the start of the training stage, meaning the observed trajectories were resampled and then forecasted. Figure 2 displays the ensemble simulation data, model predictions and epistemic errors for the formation energy, the RDF $g(r)$ and the Mahalanobis uncertainty (5). The RDF reflects the significant growth in FCC crystal structure, as can also be directly extracted through estimation of c_{FCC} , as shown in the SM[59]. MD data used $\mathcal{M}(\mathbf{D})$, eq. (12), which closely follows the theo-

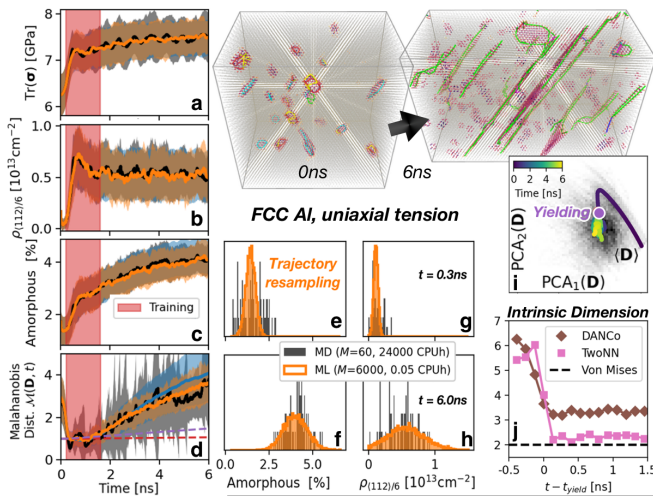


FIG. 3. Yielding of dislocation networks under uniaxial tension in Al. Color scheme follows figure 2. Forecasts are from 0.2ns, with $\tau_{tr} = 1.2ns$ and $P = 5$. Observable plots a) Pressure, b) $\langle 112 \rangle / 6$ dislocation density and c) amorphous content. d) Mahalanobis distance. e)-h) Trajectory resampling from 0.3ns (pre-yield), with $100\times$ larger ensemble. i) PCA analysis of the ensemble mean $\langle \mathbf{D} \rangle$, clearly showing a localization on yield. Individual trajectories shown as histogram in grayscale. j) ID of the descriptor manifold, estimated via the TwoNN[86] and DANCo[87] methods. Both show a collapse on yielding, but remain above the Von Mises lower bound.

retical lower bound $\mathcal{M}_\sigma(t)$. Whilst the prediction error systematically improves as training data increases in duration and diversity, of central importance is that this is reflected in the magnitude of $\mathcal{M}(\bar{\mathbf{D}}, t)$, confirming that predictions are reliable.

Yielding of Al under uniaxial tension Dislocations the agents of plastic deformation and form dense networks under irradiation[20] or extended loading[88], with atomic simulations still producing unexpected atomic mechanisms even in extensively studied pure materials[89]. Understanding yield is a central goal of metal physics[90], but atomic analysis is challenging as collective variables are elusive[36] and the dynamics are insufficiently metastable or stationary for the methods discussed above. An ensemble of $M = 60$ dense dislocation networks were formed in an EAM model of Al[91] by creating simulation boxes of around 1.5×10^5 atoms, orientated to $[10\bar{1}]$, $[111]$, $[12\bar{1}]$, with populations of interstitial loops. The initial dislocation densities spanned the typical MD range[17, 89] of $\rho_{dis} \in [10^{11}, 10^{13}]cm^{-2}$. Uniaxial tension was applied at a rate $\dot{\epsilon}_{xx} = 1 \times 10^8 s^{-1}$ along $[10\bar{1}]$, allowing other supercell dimensions to relax[17]. The SM[59] shows application to cyclic shear loading. The results are summarized in figure 3a)-d), using the linear estimators (2). Increasing τ_{tr} decreased error and uncertainty- convergence tests showed optimal results with $P = 5$ [59]. Training only on pre-yield structures led to unstable forecasts as yield is characterized by a qual-

itative change in the descriptor manifold as detailed below. However, $\mathcal{M}(\bar{\mathbf{D}}, t)$ also diverged at the yield point, clearly indicating that more training data is required. This again demonstrates the utility and critical importance of a forecast uncertainty to assess data-driven predictions. Resampling allows for ensembles to be increased by orders of magnitude for negligible CPU effort, giving smooth microstructure distributions as shown in figure 3e)-h). Initial descriptor states were generated as described above from $\rho_{tr} \simeq \mathcal{N}(\boldsymbol{\mu}_0, \boldsymbol{\Sigma}_0)$, fit from the descriptor ensemble at times 0.3-0.31ns. The forecasted ensemble captures multiple important microstructural evolutions that, whilst known for this well-studied system[17], confirm the accuracy of the VAR approach. Forecasts correctly predict the growth of amorphous atomic environments due to defect production under continued loading[92], the expected sharp peak in HCP content at yield, accompanied by a growth, peak then steady state in the number of dislocation junctions (see SM[59]). Distributions can tighten or widen, here indicating the evolution in dislocation character- initial populations of $\langle 100 \rangle / 3$ Hirth dislocation loops decay to a tight distribution close to zero upon loading, accompanied by an emergence of a broad, stable distribution of $\langle 112 \rangle / 6$ dislocation lines that carry the plastic flow[17]. The joint stability of junctions, dislocation density and stress is consistent with a Kocks-Mecking steady state[93]. The descriptor data is highly sensitive to yielding; figure 3i) shows the first two PCA components of the ensemble mean $\langle \mathbf{D} \rangle$, revealing a clear localization after yielding which can be easily classified (see SM[59]). Theoretical models for yielding invoke the concept of a yield surface in 5D stress space[94], which for metallic systems is typically the Von Mises yield surface, isosurfaces of the J_2 invariant with intrinsic dimension (ID)[58, 87] of 2. Yielding is thus expected to be accompanied by an abrupt drop in the intrinsic dimensionality of the stress trajectory. As stresses are essentially deterministic from descriptors, the descriptor ID is an upper bound to the yield surface ID. Two empirical ID estimators[86, 87, 95] were applied to the full descriptor data $\bar{\mathbf{D}} \oplus \bar{\mathbf{V}}$. Figure 3j) shows the estimated ID collapses from around 5-7 to around 2-3 on yield. Although these typically underestimate[87], this is consistent with a Von Mises ID lower bound of 2. Furthermore, this indicates the existence of a yield manifold in descriptor space, generalizing the yield surface concept to a much richer description of microstructure than stress alone. It is speculated that the yield manifold provides a route for data-driven construction of advanced structure-property relationships.

Conclusions This contribution has promoted scalar and matrix-valued descriptors as a compressed representation of atomic microstructure ideal for analysis, resampling and forecasting of simulations, with a robust forecast uncertainty derived using outlier distances. Analysis of the descriptor manifold indicates the existence of a gener-

alized yield surface, a promising direction for future research, alongside the use of forecasting in autonomous resource allocation[4, 21–25] and extension to a spatially dependent, fully equivariant descriptor framework.

ACKNOWLEDGMENTS

I thank M-C Marinica and L Truskinovsky for stimulating discussions, an anonymous referee for careful read-

ing of the manuscript, the ANR grant ANR-19-CE46-0006-1, IDRIS allocations A0090910965, A0120913455, and Euratom grant No 633053.

SUPPLEMENTARY MATERIAL FOR ‘COARSE-GRAINING AND FORECASTING ATOMIC SIMULATIONS OF SOLIDS WITH DESCRIPTOR FUNCTIONS’

Choice of descriptor function basis

Descriptors which approximate a many-body atomic basis[48–52] have found use in *linear* (LML) models $\mathcal{O} = \Theta_{\mathcal{O}} \cdot \sum_i \mathbf{D}_i$ of some target \mathcal{O} , where $\Theta_{\mathcal{O}} \in \mathbb{R}^D$ is a vector of parameters [96]. A number of possible basis functions have been proposed; an approximate classification can be made into ‘compact’ spectral expansions of 50-200 terms[48, 50] and ‘non-compact’ polynomial expansions of 1000-10000 terms, which offer greater accuracy but must be carefully regularised to avoid overfitting[49, 51, 52]. In this work, the bSO(4) bispectral descriptor functions are used[48, 50, 65], as implemented in the MILADY potential package, first introduced as part of the SNAP family of LML potentials [48]. Briefly, let $B_{ji}(\mathbf{X}), j \in [0, N_B]$ be the N_B bispectral components for an atom i , along with a constant component $B_{0i} \equiv 1$. Only neighboring atoms within the cutoff distance (here 4.7 Å) are included in the descriptor function calculation, which for the atom i reads

$$\mathbf{D}_i(\mathbf{X}) = \sum_i \bigoplus_j B_{ji}(\mathbf{X}) \in \mathbb{R}^{N_B}, \quad (6)$$

where \oplus indicates concatenation, giving $(N_B + 1)$ components. The number of bispectrum components N_B is determined by an angular momentum parameter j_{max} , here set to 4, giving $N_B = 55$.

Descriptor estimation of correlation functions

As discussed in the main text, it is also possible to predict the value of correlation functions such as the radial distribution function $g(r)$, which could be written as $g(r; \mathbf{X})$, as it is deterministic from a given set of positions \mathbf{X} . Our goal is to make a basis expansion

$$g(r; \mathbf{X}) = \sum_l a_l(\mathbf{X}) u_l(r), \quad (7)$$

where $u_l(r)$ are linearly independent. As the coefficients $a_l(\mathbf{X})$ are deterministic scalar functions of \mathbf{X} they are valid targets for estimation by a descriptor estimator $\hat{a}_l(\mathbf{D})$. In practice, $g(r; \mathbf{X})$ is evaluated up to a multiplicative constant as a histogram with a vector of H counts $\mathbf{g}(\mathbf{X}) \in \mathbb{Z}_+^H$ in H bins with centers \mathbf{r} . Fixing \mathbf{r} , an appropriate discrete basis $\mathbf{u}_l \in \mathbb{R}^H$ can be found through singular value decomposition of the rectangular matrix of T training points $\mathbf{G} = [\mathbf{g}(\mathbf{X}_1), \mathbf{g}(\mathbf{X}_2), \dots] \in \mathbb{R}^{T \times H}$. It is then simple to learn the coefficient estimators $\hat{a}_l(\mathbf{D})$ for as many singular vectors as required, which in practice was found to be 4 or 5. It is noted that $g(r)$ was only considered as an observable after simulations has been run; this is a key advantage of the current approach, as adding $g(r)$ did not require any new data generation, only estimator training on the 1% of retained positions then prediction on the full descriptor dataset. This ability to select coarse-graining targets *a posteriori* is a central advantage of the current method.

Regression of matrix-valued observables

As discussed in the main text, the descriptor vectors are then summed to give the extensive vectors $\bar{\mathbf{D}} = \sum_i \mathbf{D}_i$, $\bar{\mathbf{V}} = [\sum_i \mathbf{X}_i \otimes \nabla_{\mathbf{x}} \mathbf{D}_i]$ where $\hat{\mathbf{e}}_\alpha, \hat{\mathbf{e}}_\beta \in \mathbb{R}^3$ are Cartesian axes and \otimes is the outer (dyadic) product. In principle, the scalar $\bar{\mathbf{D}}$ are sufficient to regress scalar projections of matrix quantities such as shear stresses $\sigma_{xy} = \mathbf{e}_x \cdot \boldsymbol{\sigma} \cdot \mathbf{e}_y$. However, whilst not used in the main text, it is possible to form scalar projections $\bar{\mathbf{V}}_{\alpha\beta} = \bar{\mathbf{V}} : \mathbf{e}_\alpha \otimes \mathbf{e}_\beta$. It is then possible to regress shear stress components $\sigma_{xy} = \mathbf{e}_x \cdot \boldsymbol{\sigma} \cdot \mathbf{e}_y$. The effect of this can be seen in figure 4. It is possible

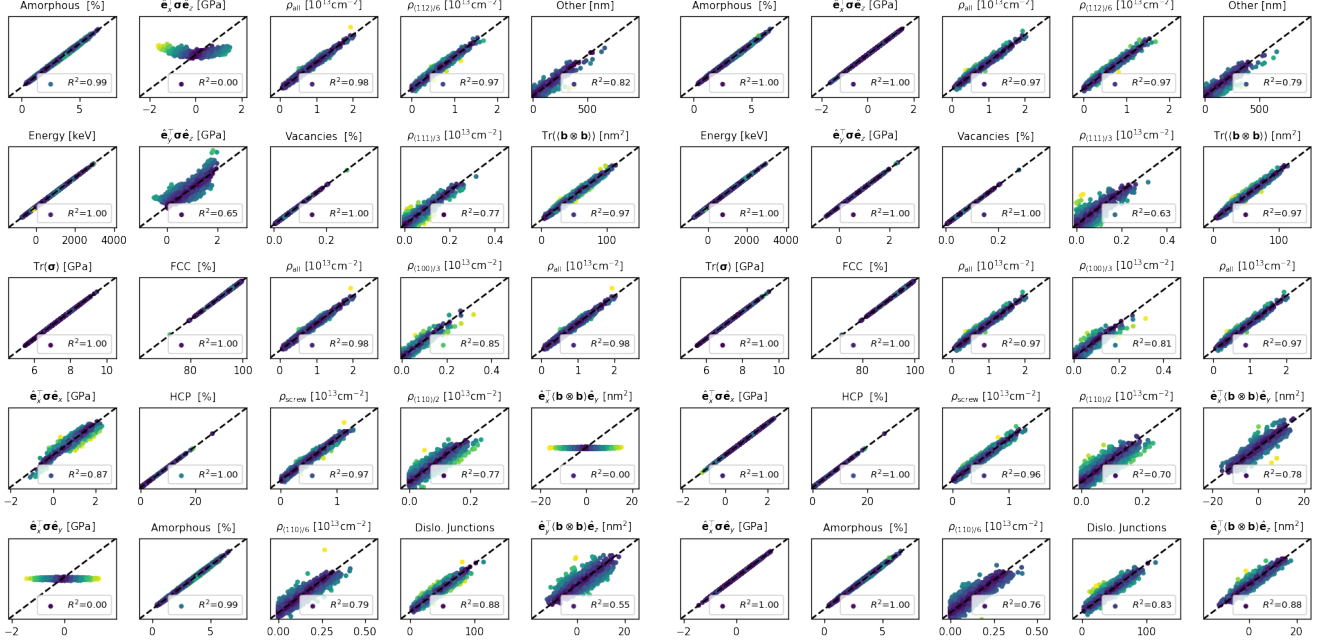


FIG. 4. Linear models with 50 components from PCA of $\bar{\mathbf{D}}$ (left) and 150 components from PCA on $\bar{\mathbf{D}} \oplus \bar{\mathbf{V}}$. Data is for the Al under uniaxial loading presented in the main text, with the same training regime.

to form matrix-equivariant linear models using only scalar coefficients $\hat{\Theta} = \Theta^\top \bar{\mathbf{V}}$, shown in figure 5. Use of $\bar{\mathbf{D}} \oplus \bar{\mathbf{V}}$ as in figure 4 gave slightly superior results; future work will investigate equivariant use of $\bar{\mathbf{D}}$ e.g. $\hat{\Theta} = \Theta^\top \bar{\mathbf{V}} + \bar{\mathbf{D}}^\top \Phi \bar{\mathbf{V}}$.

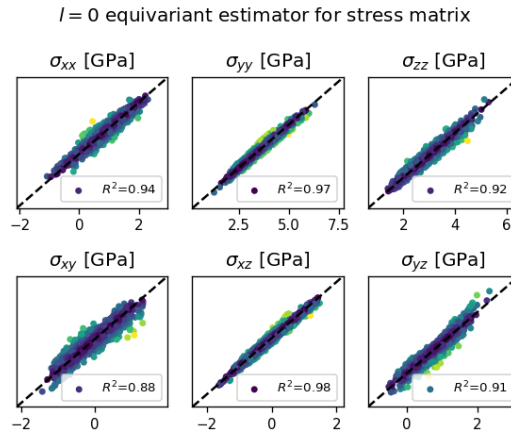


FIG. 5. Matrix-equivariant ($l = 0$ coefficients) model for the stress $\hat{\sigma} = \Theta^\top \bar{\mathbf{V}}$. Data is for the Al under uniaxial loading presented in the main text.

P-convergence of VAR models

In addition to Chapman-Komologorov tests (see below) it is also simple to study convergence in model predictions with the memory P . As can be seen in figure 6, the predictions are stable and mildly improve with increasing P .

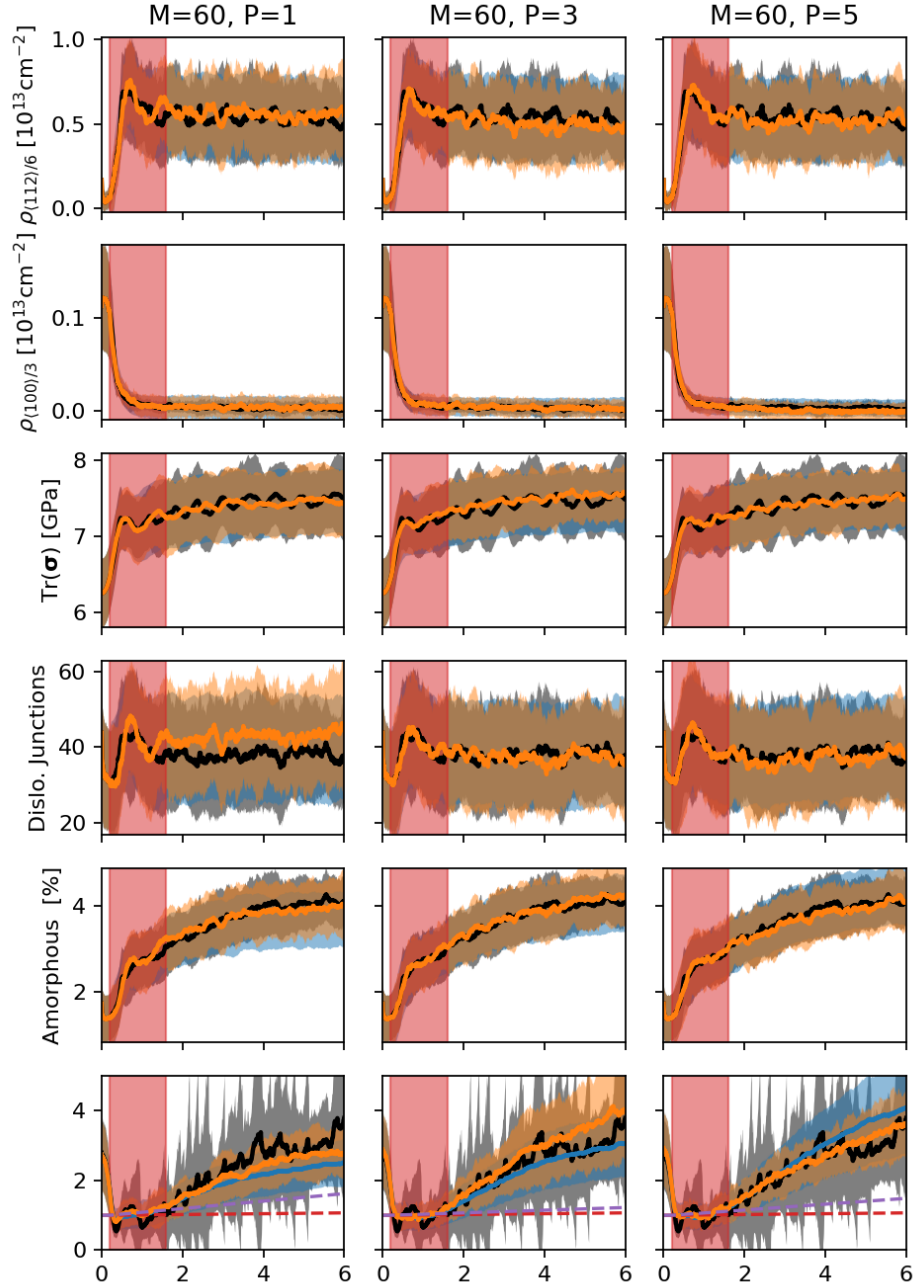


FIG. 6. Convergence test of VAR approach for Dislocation networks in Al under uniaxial tension, as presented in the main text. Left-right: VAR models with $P = 1, 3, 5$. $P = 5$ was used in the main text.

Chapman-Komologorov tests

VAR models with $P = 1$ are equivalent to extended dynamic mode decomposition[97], for which a Chapman-Komologorov test is possible. In general, in implied timescales $\omega = \ln |\lambda_\tau|/\tau$ should be a constant. As can be seen, this is satisfied for $\tau > 10$ ps.

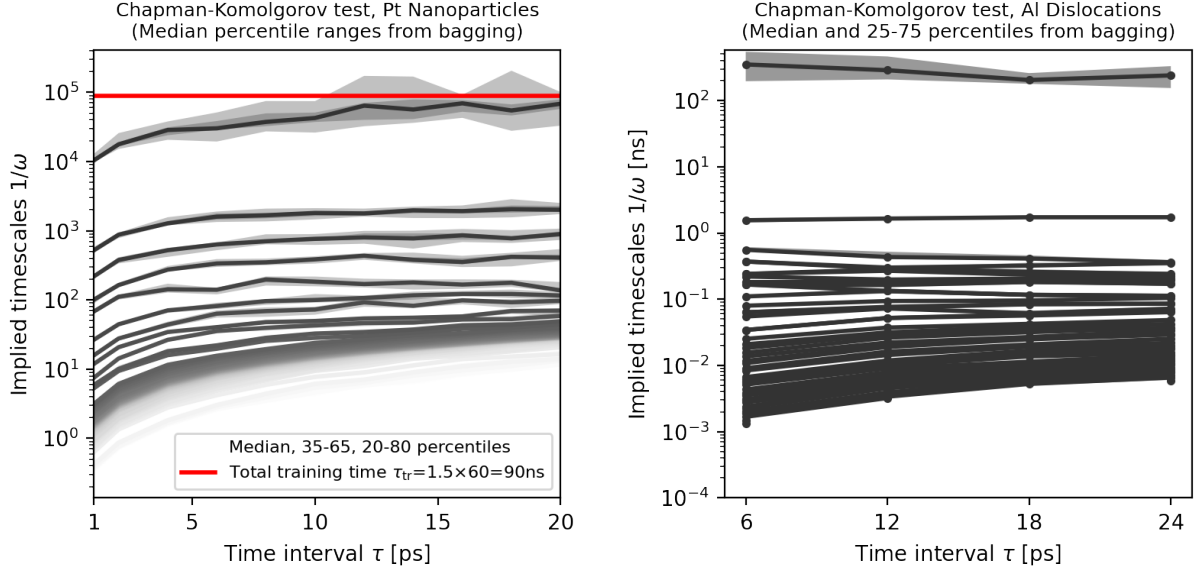


FIG. 7. Chapman-Komologorov test, $\omega = \ln |\lambda_\tau|/\tau$, for the Pt nanoparticle and Al dislocation ensembles. The implied timescales $1/\omega$ are constant for $\tau \geq 10$ ps, which is the employed interval.

Steady state of autoregressive models

The VAR(P) vector autoregressive model reads[57]

$$\tilde{\mathbf{D}}_n = \sum_{p=1}^P \mathbf{T}_p \tilde{\mathbf{D}}_{n-p} + \mathbf{c} + \delta \mathbf{W}_n, \quad \langle \delta \mathbf{W}_n^\top \delta \mathbf{W}_m \rangle = \mathbf{S} \delta_{nm}. \quad (8)$$

Consider the vector $\mathbf{Z}_{n-1} = [\tilde{\mathbf{D}}_{n-1}, \dots, \tilde{\mathbf{D}}_{n-p}]$. It satisfies the extended VAR(1) model via a Wold transformation[71]

$$\mathbf{Z}_n = \begin{bmatrix} \mathbf{T}_1 & \dots & \mathbf{T}_p \\ \mathbb{I} & \mathbf{0} & \dots \\ \mathbf{0} & \mathbb{I} & \dots \\ \mathbf{0} & \vdots & \dots \\ \dots & \mathbb{I} & \mathbf{0} \end{bmatrix} \mathbf{Z}_{n-1} + \begin{bmatrix} \mathbf{c} + \delta \mathbf{W}_n \\ \mathbf{0} \\ \mathbf{0} \\ \vdots \\ \mathbf{0} \end{bmatrix} = \mathbf{T}_Z \mathbf{Z}_n + \delta \mathbf{Y}_n. \quad (9)$$

We can now solve for the steady state as for any other VAR(1), or Ornstein-Uhlenbeck equation[72], with a Gaussian steady state

$$\lim_{t \rightarrow \infty} \rho(\mathbf{Z}, t) = \mathcal{N}(\mathbf{Z}_\infty, \mathbf{Q}_\infty) \quad (10)$$

where

$$[\mathbb{I} - \mathbf{T}_Z] \mathbf{Z}_\infty \equiv \mathbf{c}, \quad \mathbf{S} = \mathbf{L}^\top \mathbf{L}, \quad [\mathbb{I} - \mathbf{T}_Z] \mathbf{V} = \mathbf{L}, \quad \mathbf{Q}_\infty = \mathbf{V}^\top \mathbf{V}, \quad (11)$$

where we express the mean and variance in a form which allows for a null space of $[\mathbb{I} - \mathbf{T}_Z]$ in the case of inadequate training data or underregularisation[98].

Unimodality of descriptor distributions

As discussed in the text, the error metrics we employ rely on approximately unimodal descriptor distributions. Figure (8) shows the descriptor datasets used for the forecasting model, the raw descriptor data reduced to 50 dimensions and whitened (decorrelated) through application of the PCA technique[98]. As can be seen, the histograms are unimodal to a high degree of approximation. The only slight deviation came from one component for the Pt nanoparticles, but we attribute this primarily to the relatively small sample size of 60 simulation workers in a small atomic system. For the Al dislocation system, the unimodality is clear.

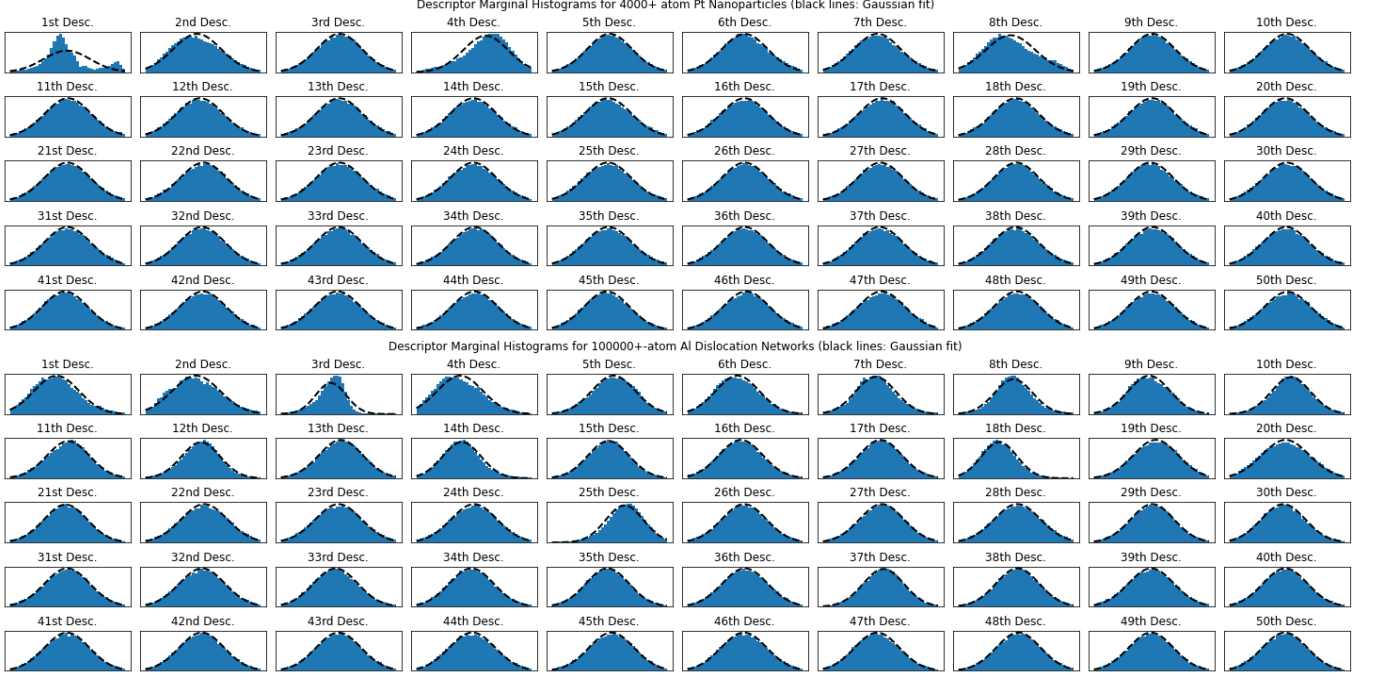


FIG. 8. Descriptor histograms for the Pt nanoparticles (top) and Al histograms (bottom).

Uncertainty propagation to the Mahalanobis distance

The bagging regression procedure detailed in the main text returns expectation values and covariances for model parameters $\mathbf{T}_z, \mathbf{c}, \mathbf{S}$. In practice, we decompose $\mathbf{S} = \mathbf{X}^\top \text{Diag}(\boldsymbol{\lambda}) \mathbf{X}$ and only consider covariance of the positive eigenvalues $\boldsymbol{\lambda}$. Epistemic uncertainties in \mathbf{T}_z where found to have negligible influence and thus are not considered here. These parameter uncertainties, expressed by the covariances $\boldsymbol{\Sigma}_c$ and $\boldsymbol{\Sigma}_\lambda$ of \mathbf{c} and $\boldsymbol{\lambda}$, will induce a random perturbation on the square Mahalanobis distance

$$\mathcal{M}(\bar{\mathbf{D}}) = [\bar{\mathbf{D}} - \boldsymbol{\mu}_{\text{tr}}] \boldsymbol{\Sigma}_{\text{tr}}^{-1} [\bar{\mathbf{D}} - \boldsymbol{\mu}_{\text{tr}}] / \bar{D}. \quad (12)$$

As discussed in the main text, as this uncertainty always increases \mathcal{M} it cannot be assumed to be a mean zero fluctuation and thus should be accumulated, leading to a linear growth in time. It is simple to propagate this uncertainty to $\mathcal{M}(\bar{\mathbf{D}})$:

$$\sigma_{\mathcal{M}}^2 = \text{Tr} \left([\mathbb{I} - \mathbf{T}_z]^{-1} \boldsymbol{\Sigma}_c \boldsymbol{\Sigma}_{\text{tr}}^{-1} \right) / \bar{D} + \text{Tr} \left([\mathbb{I} - \mathbf{T}_z]^{-1} \mathbf{X}^\top \boldsymbol{\Sigma}_\lambda \mathbf{X} \boldsymbol{\Sigma}_{\text{tr}}^{-1} \right) / \bar{D} \quad (13)$$

In practice, we ensure that $\sigma_{\mathcal{M}}^2 > \delta\tau/\tau_M$ though the mapping $\sigma_{\mathcal{M}}^2 \rightarrow 1/(1/\sigma_{\mathcal{M}}^2 + \tau_M/\delta\tau)$, though as can be seen in the figures the addition of this has only a very minor influence on the expected uncertainty.

Yielding of dislocation networks under cyclic shear

An ensemble of $M = 60$ dense dislocation networks were formed in an EAM model of Al[91] by creating simulation boxes of around 1.5×10^5 atoms, orientated to $[10\bar{1}]$, $[111]$, $[1\bar{2}1]$, with populations of interstitial loops. The initial dislocation densities spanned the range typically found in MD[17, 89], $\rho_{\text{dis}} \in [10^{11}, 10^{13}] \text{cm}^{-2}$. Ensembles were subjected to cyclic shearing at a rate $|\dot{\epsilon}_{xy}| = 1 \times 10^8 \text{s}^{-1}$ up to $|\epsilon_{xy}| = 0.1$ with a sawtooth profile for a total of two cycles. As can be seen, the initially disperse dislocation densities across the ensemble tightens after a few cycles, as the driven steady state emerges.

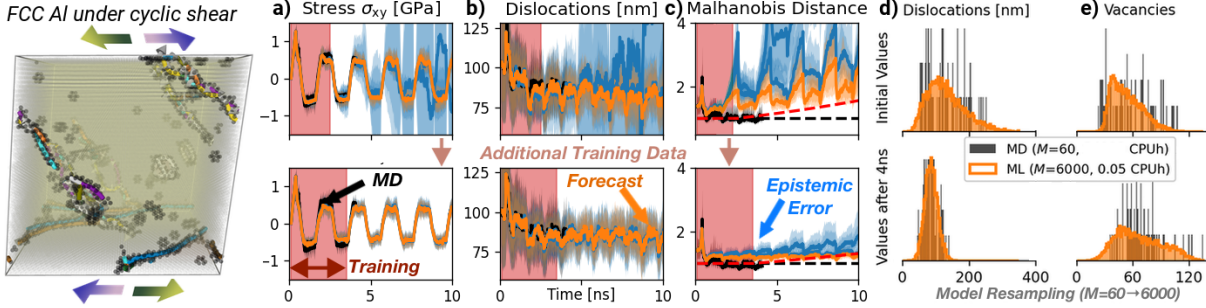


FIG. 9. Cyclic shearing of dislocation networks in Al. Left: Representative simulation supercell. a)-c): Forecasts using 2.5ns (top) and 3ns (bottom) for training and resampling, showing a) shear stress, b) total dislocation density and c) outlier distance. For lower training data the outlier distance is clearly seen to spike at yield points, these being the least sampled configurations. d)-e): resampling, increasing the effective ensemble size one hundredfold. The total dislocation density distribution d) noticeably tightens. demonstrating a convergence to a driven steady state, whilst the vacancy distribution e) slightly widens, most likely due to defect generation at high strain rates.

Classification of yield

A simple linear support vector machine (SVM)[98] classifier was trained on 25% of trajectories around the yield point. As can be seen in figure 10, the transferability to new trajectories shows excellent accuracy, both in pointwise comparison (left) and distributionwise (right).

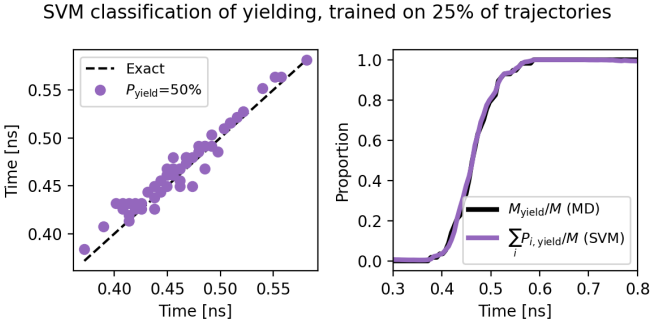


FIG. 10. SVM classification of yielding. Left: scatter plot of time at yield vs predicted time at 50% probability. Right: observed and predicted proportion of yielded trajectories.

* thomas.swinburne@cnrs.fr

[1] D. J. Wales, *Energy Landscapes*, edited by C. U. Press (Cambridge, 2003).
 [2] D. Perez, B. P. Uberuaga, Y. Shim, J. G. Amar, and A. F. Voter, *Annual Reports in computational chemistry* **5**, 79 (2009).

- [3] S. Plimpton, *Journal Computational Physics* **117**, 1 (1995).
- [4] D. Perez, E. D. Cubuk, A. Waterland, E. Kaxiras, and A. F. Voter, *Journal of chemical theory and computation* **12**, 18 (2015).
- [5] A. Laio and M. Parrinello, *Proceedings of the National Academy of Sciences* **99**, 12562 (2002).
- [6] A. Mardt, L. Pasquali, H. Wu, and F. Noé, *Nature communications* **9**, 1 (2018).
- [7] E. Van Der Giessen, P. A. Schultz, N. Bertin, V. V. Bulatov, W. Cai, G. Csányi, S. M. Foiles, M. G. Geers, C. González, M. Hütter, *et al.*, *Modelling and Simulation in Materials Science and Engineering* **28**, 043001 (2020).
- [8] L. Bonati, G. Piccini, and M. Parrinello, *Proceedings of the National Academy of Sciences* **118**, e2113533118 (2021).
- [9] T. D. Swinburne and D. Perez, *Modelling and Simulation in Materials Science and Engineering* **30**, 034004 (2022).
- [10] J. D. Honeycutt and H. C. Andersen, *Journal of Physical Chemistry* **91**, 4950 (1987).
- [11] C. L. Kelchner, S. J. Plimpton, and J. C. Hamilton, *Phys. Rev. B* **58**, 11085 (1998).
- [12] G. J. Ackland and A. P. Jones, *Phys. Rev. B* **73**, 054104 (2006).
- [13] E. A. Lazar, J. K. Mason, R. D. MacPherson, and D. J. Srolovitz, *Phys. Rev. Lett.* **109**, 095505 (2012).
- [14] E. A. Lazar, J. Han, and D. J. Srolovitz, *Proceedings of the National Academy of Sciences* **112**, E5769 (2015).
- [15] A. Stukowski, V. V. Bulatov, and A. Arsenlis, *Modelling and Simulation in Materials Science and Engineering* **20**, 085007 (2012).
- [16] G. Wu, H. Song, and D. Lin, *Computational Materials Science* **144**, 322 (2018).
- [17] L. A. Zepeda-Ruiz, A. Stukowski, T. Ooppelstrup, and V. V. Bulatov, *Nature* **550**, 492 (2017).
- [18] W. Setyawan, G. Nandipati, K. J. Roche, H. L. Heinisch, B. D. Wirth, and R. J. Kurtz, *Journal of Nuclear Materials* **462**, 329 (2015).
- [19] N. V. Priezjev, *Journal of Non-Crystalline Solids* **479**, 42 (2018).
- [20] D. R. Mason, S. Das, P. M. Derlet, S. L. Dudarev, A. J. London, H. Yu, N. W. Phillips, D. Yang, K. Mizohata, R. Xu, *et al.*, *Physical Review Letters* **125**, 225503 (2020).
- [21] T. Swinburne and D. Perez, *npj Computational Materials* **6**, 190 (2020).
- [22] A. Garmon, V. Ramakrishnaiah, and D. Perez, *Parallel Computing*, 102936 (2022).
- [23] J. Schaarschmidt, J. Yuan, T. Strunk, I. Kondov, S. P. Huber, G. Pizzi, L. Kahle, F. T. Bölle, I. E. Castelli, T. Vegge, *et al.*, *Advanced Energy Materials* **12**, 2102638 (2022).
- [24] L.-F. Zhu, J. Janssen, S. Ishibashi, F. Körmann, B. Grabowski, and J. Neugebauer, *Computational Materials Science* **187**, 110065 (2021).
- [25] J. Andrews, O. Gkoutouna, and E. Blaisten-Barojas, *Chemical Science* **13**, 7021 (2022).
- [26] C. Le Bris, T. Lelièvre, M. Luskin, and D. Perez, *Monte Carlo Methods and Applications* **18**, 119 (2012).
- [27] A. F. Voter, *Physical Review B* **57**, R13985 (1998).
- [28] G. Henkelman and H. Jónsson, *The Journal of chemical physics* **111**, 7010 (1999).
- [29] M. So and A. Voter, *The Journal of Chemical Physics* **112**, 9599 (2000).
- [30] A. F. Voter, *Physical Review Letters* **78**, 3908 (1997).
- [31] G. Henkelman, B. P. Uberuaga, and H. Jónsson, *The Journal of Chemical Physics* **113**, 9901 (2000).
- [32] E. Darve, D. Rodríguez-Gómez, and A. Pohorille, *The Journal of chemical physics* **128**, 144120 (2008).
- [33] T. Lelièvre, G. Stoltz, and M. Rousset, *Free energy computations: A mathematical perspective* (World Scientific, 2010).
- [34] T. D. Swinburne and M.-C. Marinica, *Phys. Rev. Lett.* **120**, 135503 (2018).
- [35] J. Rogal, *The European Physical Journal B* **94**, 1 (2021).
- [36] J. Baima, A. S. Goryaeva, T. Swinburne, J.-B. Maillet, M. Nastar, and M. C. Marinica, *Phys. Chem. Chem. Phys.*, (2022).
- [37] G. Bussi and A. Laio, *Nature Reviews Physics* **2**, 200 (2020).
- [38] F. Noé and F. Nuske, *Multiscale Modeling & Simulation* **11**, 635 (2013).
- [39] R. Huang, L.-T. Lo, Y. Wen, A. Voter, and D. Perez, *The Journal of chemical physics* **147**, 152717 (2017).
- [40] R. Huang, Y. Wen, A. Voter, and D. Perez, *Physical Review Materials* **2**, 126002 (2018).
- [41] T. Xie, A. France-Lanord, Y. Wang, Y. Shao-Horn, and J. C. Grossman, *Nature communications* **10**, 1 (2019).
- [42] S. Soltani, C. W. Sinclair, and J. Rottler, *Phys. Rev. E* **106**, 025308 (2022).
- [43] W. Wang and R. Gómez-Bombarelli, *npj Computational Materials* **5**, 125 (2019).
- [44] L. Klein, A. Y. Foong, T. E. Fjelde, B. Mlodozieniec, M. Brockschmidt, S. Nowozin, F. Noé, and R. Tomioka, *arXiv preprint arXiv:2302.01170* (2023).
- [45] C. Han, P. Zhang, D. Bluestein, G. Cong, and Y. Deng, *Journal of Computational Physics* **427**, 110053 (2021).
- [46] B. Leimkuhler, D. T. Margul, and M. E. Tuckerman, *Molecular Physics* **111**, 3579 (2013).
- [47] X. Fu, T. Xie, N. J. Rebello, B. D. Olsen, and T. Jaakkola, *arXiv preprint arXiv:2204.10348* (2022).
- [48] A. P. Thompson, L. P. Swiler, C. R. Trott, S. M. Foiles, and G. J. Tucker, *J. Comp. Phys.* **285**, 316 (2015).
- [49] A. Shapeev, *Multiscale Model. Sim.* **14**, 1153 (2016).
- [50] A. M. Goryaeva, J. Dérès, C. Lapointe, P. Grigorev, T. D. Swinburne, J. R. Kermode, L. Ventelon, J. Baima, and M.-C. Marinica, *Phys. Rev. Materials* **5**, 103803 (2021).
- [51] A. E. Allen, G. Dusson, C. Ortner, and G. Csányi, *Machine Learning: Science and Technology* **2**, 025017 (2021).
- [52] Y. Lysogorskiy, C. van der Oord, A. Bochkarev, S. Menon, M. Rinaldi, T. Hammerschmidt, M. Mrovec, A. Thompson, G. Csányi, C. Ortner, *et al.*, *npj Computational Materials* **7**, 1 (2021).
- [53] P. C. Mahalanobis (National Institute of Science of India, 1936).
- [54] E. V. Podryabinkin and A. V. Shapeev, *Computational Materials Science* **140**, 171 (2017).
- [55] N. Bernstein, G. Csányi, and V. L. Deringer, *npj Computational Materials* **5**, 1 (2019).

- [56] A. M. Goryaeva, C. Lapointe, C. Dai, J. Dérès, J.-B. Maillet, and M.-C. Marinica, *Nat. Commun.* **11**, 4691 (2020).
- [57] H. Lütkepohl, *New introduction to multiple time series analysis* (Springer Science & Business Media, 2005).
- [58] A. Glielmo, I. Macocco, D. Doimo, M. Carli, C. Zeni, R. Wild, M. d’Errico, A. Rodriguez, and A. Laio, *Patterns* **3**, 100589 (2022).
- [59] Supplementary Material.
- [60] V. L. Deringer, M. A. Caro, and G. Csányi, *Advanced Materials* **31**, 1902765 (2019).
- [61] A. P. Bartók, S. De, C. Poelking, N. Bernstein, J. R. Kermode, G. Csányi, and M. Ceriotti, *Sci. Adv.* **3**, e1701816 (2017).
- [62] I. Batatia, D. P. Kovács, G. N. Simm, C. Ortner, and G. Csányi, arXiv preprint arXiv:2206.07697 (2022).
- [63] S. Chmiela, A. Tkatchenko, H. E. Sauceda, I. Poltavsky, K. T. Schütt, and K.-R. Müller, *Science advances* **3**, e1603015 (2017).
- [64] S. Batzner, A. Musaelian, L. Sun, M. Geiger, J. P. Mailoa, M. Kornbluth, N. Molinari, T. E. Smidt, and B. Kozinsky, *Nature communications* **13**, 1 (2022).
- [65] A. P. Bartók, M. C. Payne, R. Kondor, and G. Csányi, *Phys. Rev. Lett.* **104**, 136403 (2010).
- [66] In practice, the tensor of symmetric matrices $\bar{\mathbf{V}}_s \equiv \bar{\mathbf{V}} + \bar{\mathbf{V}}^T$ is calculated in current implementations[3, 50].
- [67] C. Lapointe, T. D. Swinburne, L. Thiry, S. Mallat, L. Proville, C. S. Becquart, and M.-C. Marinica, *Physical Review Materials* **4**, 063802 (2020).
- [68] C. Lapointe, T. D. Swinburne, L. Proville, C. S. Becquart, N. Mousseau, and M.-C. Marinica, Under Review (2022).
- [69] T. D. Swinburne, S. L. Dudarev, and A. P. Sutton, *Physical Review Letters* **113**, 215501 (2014).
- [70] S. Karlsson, *Handbook of economic forecasting* **2**, 791 (2013).
- [71] H. O. Wold, *The Annals of Mathematical Statistics* **19**, 558 (1948).
- [72] W. Coffey and Y. P. Kalmykov, *The Langevin equation: with applications to stochastic problems in physics, chemistry and electrical engineering*, Vol. 27 (World Scientific, 2012).
- [73] L. Breiman, *Machine learning* **24**, 123 (1996).
- [74] B. Lakshminarayanan, A. Pritzel, and C. Blundell, *Advances in neural information processing systems* **30** (2017).
- [75] F. Petropoulos, R. J. Hyndman, and C. Bergmeir, *European Journal of Operational Research* **268**, 545 (2018).
- [76] F. Pedregosa, G. Varoquaux, A. Gramfort, V. Michel, B. Thirion, O. Grisel, M. Blondel, P. Prettenhofer, R. Weiss, V. Dubourg, J. Vanderplas, A. Passos, D. Cournapeau, M. Brucher, M. Perrot, and E. Duchesnay, *Journal of Machine Learning Research* **12**, 2825 (2011).
- [77] Y. Yu, X. Si, C. Hu, and J. Zhang, *Neural computation* **31**, 1235 (2019).
- [78] P. R. Vlachas, J. Zavadlav, M. Praprotnik, and P. Koumoutsakos, *Journal of Chemical Theory and Computation* **18**, 538 (2021).
- [79] P. Kidger, J. Morrill, J. Foster, and T. Lyons, *Advances in Neural Information Processing Systems* **33**, 6696 (2020).
- [80] F. Liu, M. Cai, L. Wang, and Y. Lu, *IEEE Access* **7**, 26102 (2019).
- [81] C. Zeni, A. Anelli, A. Glielmo, and K. Rossi, *Physical Review B* **105**, 165141 (2022).
- [82] Y. Chen, A. Wiesel, Y. C. Eldar, and A. O. Hero, *IEEE transactions on signal processing* **58**, 5016 (2010).
- [83] T. D. Swinburne and D. Perez, *Phys. Rev. Materials* **2**, 053802 (2018).
- [84] F. Baletto, R. Ferrando, A. Fortunelli, F. Montalenti, and C. Mottet, *The Journal of chemical physics* **116**, 3856 (2002).
- [85] C. Liu, J. Cohen, J. Adams, and A. Voter, *Surface science* **253**, 334 (1991).
- [86] E. Facco, M. d’Errico, A. Rodriguez, and A. Laio, *Scientific reports* **7**, 12140 (2017).
- [87] C. Ceruti, S. Bassis, A. Rozza, G. Lombardi, E. Casiraghi, and P. Campadelli, *Pattern recognition* **47**, 2569 (2014).
- [88] S. Lavenstein, Y. Gu, D. Madisetti, and J. A. El-Awady, *Science* **370**, eabb2690 (2020).
- [89] N. Bertin, W. Cai, S. Aubry, A. Arsenlis, and V. V. Bulatov, arXiv preprint arXiv:2210.14343 (2022).
- [90] R. Baggio, E. Arbib, P. Biscari, S. Conti, L. Truskinovsky, G. Zanzotto, and O. Salman, *Physical Review Letters* **123**, 205501 (2019).
- [91] B. Onat and S. Durukanoglu, *Journal of Physics: Condensed Matter* **26**, 035404 (2013).
- [92] J. Marian, W. Cai, and V. V. Bulatov, *Nature materials* **3**, 158 (2004).
- [93] R. B. Sills, N. Bertin, A. Aghaei, and W. Cai, *Physical review letters* **121**, 085501 (2018).
- [94] J. P. Hirth and J. Lothe, *Theory Of Dislocations* (Malabar, FL Krieger, 1991).
- [95] J. Bac, E. M. Mirkes, A. N. Gorban, I. Tyukin, and A. Zinovyev, *Entropy* **23**, 1368 (2021).
- [96] Offsets are absorbed into the first entry of the per-atom descriptor \mathbf{D}_i (i.e. $D_{i1} = 1$).
- [97] M. O. Williams, I. G. Kevrekidis, and C. W. Rowley, *Journal of Nonlinear Science* **25**, 1307 (2015).
- [98] C. E. Rasmussen, *Gaussian Processes in Machine Learning* (Springer, Berlin, Heidelberg, 2004).